IEEE Open Journal of
Antennas and Propagation

Received 31 March 2022; revised 26 April 2022; accepted 2 May 2022. Date of publication 6 May 2022; date of current version 12 May 2022.

Digital Object Identifier 10.1109/OJAP.2022.3173161

3D Printed Linearly Polarized X-Band Conical Horn Antenna and Lens

IAN GOODE AND CARLOS E. SAAVEDRA

Department of Electrical and Computer Engineering, Queen's University, Kingston, ON K7L 3N6, Canada

CORRESPONDING AUTHOR: I. GOODE (e-mail: ian.goode@queensu.ca)

This work was supported in part by the Natural Sciences and Engineering Research Council of Canada (NSERC) under Grant RGPIN-2022-05204.

ABSTRACT A fast and convenient method to 3D print and metalize circular waveguide components is demonstrated using polylactic acid (PLA) and aluminum adhesive backed tape. A gradient index (GRIN) lens, an externally metalized thin-walled conical horn, and a WR90 rectangular to linearly polarized circular waveguide transition are simulated, fabricated, and measured. The horn and lens were both monolithic prints that were externally metallized to simplify the metallization process. Both the horn and lens have a measured operational bandwidth of 8.2 GHz to 12.4 GHz with an input reflection less than −15 dB and peak gain of 18.7 dBi at mid-band. The walls of the thin-wall horn are printed at a thickness such that the dielectric layer does not impact the performance of the horn while being robust enough to support external metallization. The lensed horn functioned as the support for the aluminum foil while also improving the radiation pattern by improving the $\vec{E}$ SLL by up to 15 dB compared to the thin-walled horn antenna.

INDEX TERMS 3D printing, aperture antenna, circular waveguide, dielectric lens, GRIN lens, horn antenna, waveguide, x-band.

I. INTRODUCTION

WAVEGUIDE components require smooth and highly conductive surfaces which conventionally have been achieved through expensive techniques such as machining and draw forming. Additive manufacturing has been useful to reduce the cost and lead time for designing waveguide components. 3D printing of waveguide components has been seen with metal 3D printing [1], various spray coatings and electroplating for plastic 3D printing [2]–[5], metal infused conductive plastic filaments [6], and plastic 3D prints covered in metal foil tape [7]–[10]. Multiple technologies are used for plastic 3D printing. Common methods include: selective laser sintering (SLS) where a laser is used to selectively melt and fuse a plastic (or metal) from a supply of powered substrate; fused deposition modeling (FDM) where molten plastic is extruded from a computer-controlled hot-end and cooled to form a part; and stereolithography (SLA) where a light source is used to selectively harden photo-activated resins. All these methods have been shown to provide performance that is comparable to traditionally machined waveguide components.

In addition to allowing for rapid and inexpensive prototyping, printed waveguide components can allow for lighter weight devices than machined waveguides. Waveguides can be metal 3D printed in a mesh to reduce weight while still allowing for acceptable performance [1]. By printing and metalizing waveguide components they can be made even lighter, such as an antenna that was printed into the wing of an unmanned aerial vehicle [3] or for lightweight antennas in space applications [11].

Other than printing plastics for the structure of waveguide components, many materials used for 3D printing are low loss and can be used to make lenses for antenna pattern enhancement or beam-steering. Such lenses can be in the radiation path outside of the antenna [7], [12] or as part of the antenna itself [5], [10]. Lenses are used to improve the radiation characteristics by increasing the peak gain, reducing side-lobe levels (SLL), or allowing for beam-steering. Dielectric lenses are made by varying the propagation delay through the lens to form the radiated beam to a desired shape in the far field. This beamforming is accomplished by varying the permittivity in the lens [7], [13], by changing the shape of the lens with a

homogenous dielectric material [14]–[18] or with a combination of the two [19], [20]. These lenses can be made by milling and drilling pieces of dielectric material to create the desired reduction in permittivity [14], [16], [21] but adaptive manufacturing has allowed for the easy fabrication of lenses by allowing for controlled volumes and placements of dielectric materials inside the lens to allow for geometries that are difficult to manufacture through subtractive manufacturing methods.

In this work a gradient index (GRIN) lens is made in the shape of a conical horn that also acts as the structure to support metallization to make a lensed conical horn antenna. A thin-walled externally metalized conical horn antenna, and a rectangular to circular waveguide transition are also designed and measured to give a full system from rectangular waveguide to a circular antenna. Each component is fabricated using FDM printing with PLA (polylactic acid) and metalized using adhesive backed aluminum foil tape. Each of these parts is designed to simplify the metallization using foil tape by minimizing compound bends to reduce wrinkles in the foil and externally metalizing the horn antennas so that they can be printed and metallized in a single piece. The conical GRIN lens provides the structure to support external metallization and corrects the delay through the horn to fix the high $\vec{E}$-plane SLL that are common with aperture antennas. The wall of the thin-walled PLA horn is made thin-enough to not impact the performance when compared an inner-side metalized horn of the same geometry. The transition employs a conical transition to taper the rectangular waveguide to the circular waveguide. This transition is easier to print compared to machining as it would require multiple complex machining operations. It was printed in multiple parts to minimize wrinkles when applying the aluminum tape. Each of these methods was intended to simplify the FDM printing and metallization options while giving comparable or better performance compared to more complex or costly fabrication options.

II. HORN AND LENS DESIGN

The design of the conical GRIN lens, thin-walled horn, and the rectangular to circular transition were done independently. The design of each focused on being 3D printable on a consumer-grade FDM printer and metallizable using adhesive backed aluminum tape. For all 3D-printed components D3D's Natural Tough PLA was used for its ease of printing, ability to be taped, and lack of additives for coloring which could increase the loss. The electrical properties of the PLA used in this work were validated in a K-band lens [7] and were measured using a Keysight Dielectric Probe Kit [22]. Based on these works, the PLA has $\epsilon_r = 2.7$ and negligible loss as these were seen to give good agreement between measurement and simulation. All simulations were run in ANSYS Electronics Desktop HFSS 2021 R1 and were fed with wave-ports. All simulations assumed the metallization was aluminum with a thickness of 1 mm.

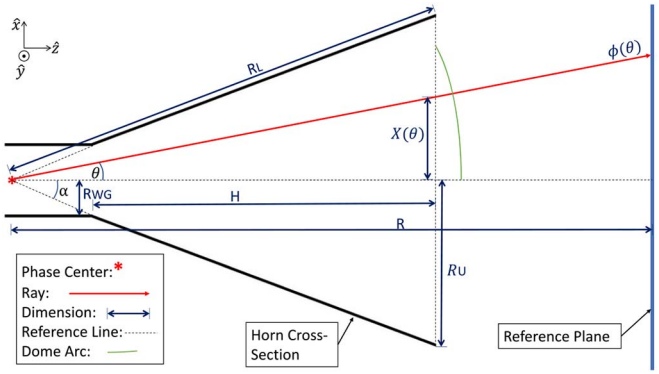

FIGURE 1. Lens delay model.

Lens Design – The conical GRIN lens was designed to be printed from PLA. The purpose of this lens was to both function as a support for the aluminum foil and to adjust the phase-delay through the lens to reduce the side-lobes that are seen in the $\vec{E}$-plane with linearly polarized horn antennas. The lens was designed to have a uniform phase delay for all angles of propagation from the phase center of the horn to a reference plane in space. This was accomplished by having a gradient of dielectric material to force slower propagation through the center of the lens compared with near the side of the horn to give a plane wave at the aperture of the lens. Since the lens and horn were radially symmetric the permittivity gradient only needed to be designed for a single cross-section of the lens. The lens was broken into two sections, a *cone* section inside the metallized horn, and a *dome* section outside of the metallization. This method was chosen to improve the impedance match going into the lens by gradually transitioning between the highest permittivity in the lens ($\epsilon_{r_{center}}$) and free-space in the $\hat{z}$ direction. Additionally, this method of defining the permittivity gradient inside the lens allowed the gradient to be defined as a function that only varied with the radius of the lens at the horn's aperture, thereby simplifying the problem.

The permittivity gradient in the lens was designed by finding a relation between delay to a reference plane from the phase center of the horn antenna as shown in Fig. 1 and eqns. (1) – (9) for a permittivity function that varied as the radius of the horn at its aperture, where $\phi(\theta)$ is the delay for a given ray from the phase center of the horn to a reference plane in the main radiation direction. The lens was designed as a cone inside the horn, and a dome that protruded past the limits of metallization. The permittivity was varied as a function of radius at the aperture of the horn, to map a point onto this gradient the two mapping functions in eqn. (2) and (5) were used. The dome section mapping function eqn. (2) is a trigonometric to map a point on the gradient inside the cone section of the lens to the radius at the aperture of the horn. The dome mapping function in eqn. (5) maps a point on an arc (as shown in Fig. 1) from the center line of the lens to a given radius at the aperture of the horn. Each of these arcs have the same radius and the

center point of the gradient arcs are moved in the $\hat{z}$-direction to stack the arcs to create the gradient shown in Fig. 2 (a).

$$\phi_{cone}(\theta) = \int_0^{\frac{R_U}{\tan\alpha\cos\theta}} n(X_{cone}(r,\theta))\,dr \tag{1}$$

$$X_{cone}(r,\theta) = RL\sin\theta \tag{2}$$

$$\alpha = \arctan\left(\frac{R_U - R_{WG}}{H}\right) \tag{3}$$

$$\phi_{dome}(\theta) = \int_{\frac{R_U}{\tan\alpha\cos\theta}}^{RL} n(X_{dome}(r,\theta))\,dr \tag{4}$$

$$X_{dome}(r,\theta) = \sqrt{\left(\frac{R_U}{\sin\alpha}\right)^2 - \kappa(r,\theta)^2} \tag{5}$$

$$\kappa(r,\theta) = \frac{R_U}{\tan\alpha} - r\cos\theta + \xi(r,\theta) \tag{6}$$

$$\xi(r,\theta) = \sqrt{\left(\frac{R_U}{sin\alpha}\right)^2 - r\sin\theta} \tag{7}$$

$$\phi_{space}(\theta) = \int_{RL}^{\frac{R}{\cos\theta}} n_0\,dr \tag{8}$$

$$\phi(\theta) = \phi_{cone}(\theta) + \phi_{dome}(\theta) + \phi_{space}(\theta) \tag{9}$$

Once the total delay was defined in eqn. (9) for a given angle θ that related the delay to the reference plane to a gradient of permittivity in the lens that varied as a function of the lens's radius at the aperture of the horn, a gradient index function in eqn. (10) was chosen to fit the permittivity gradient. The fitting parameters A and B were chosen to equalize all $\phi(\theta)$ for $0 \le \theta \le \alpha$ with value of the permittivity at the center of the lens $\epsilon_{r_{center}}$ chosen to minimize the reflections at the lens to improve the impedance match. Eqn. (10) was fitted by numerically solving all the expressions in eqns. (1) – (10) and then solving the optimization problem to find the best values for A and B for a given $\epsilon_{r_{center}}$. $\epsilon_{r_{center}} = 1.7$ was chosen as a compromise between minimizing reflections through the lens and maintaining a large enough minimum permittivity that it would still be printable at the edges of the lens and provide adequate support for the aluminum foil.

$$n(X) = A(\cosh(BX) - 1) + \sqrt{\epsilon_{r_{center}}} \tag{10}$$

$$\epsilon_r(X) = n(X)^2 \tag{11}$$

The chosen permittivity gradient can be visualized in a cross section of the radially symmetric GRIN lens in Fig. 2 (a) with the function describing permittivity gradient shown in Fig. 2 (b). This lens was simulated as 19 discrete shells of varying permittivity in HFSS. These shells are shown as the discrete steps in permittivity seen in Fig. 2 (a). Fig. 3 shows how the lens drastically reduced the shoulders in the $\vec{E}$-plane versus a simple circular horn and Fig. 4 shows fields propagating through the lens and a horn. Here the phase fronts in the lens are seen to slow the propagation at the center of the lens to create a plane wave once the fields exit the lens.

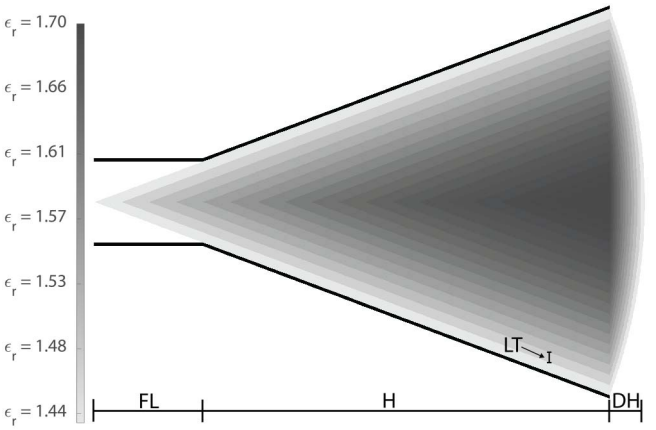

(a)

var.	FL	H	DH	LT
[mm]	25	120	10.4	3

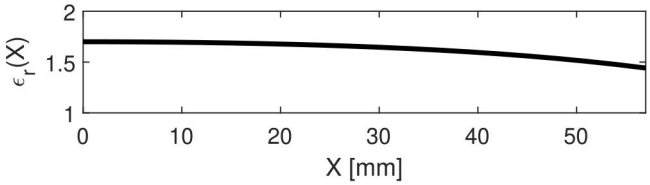

(b)

FIGURE 2. (a) Cross section of the lensed antenna showing the gradient of the permittivity shells in the lens, (b) plot of the continuous gradient permittivity as a function of horn radius.

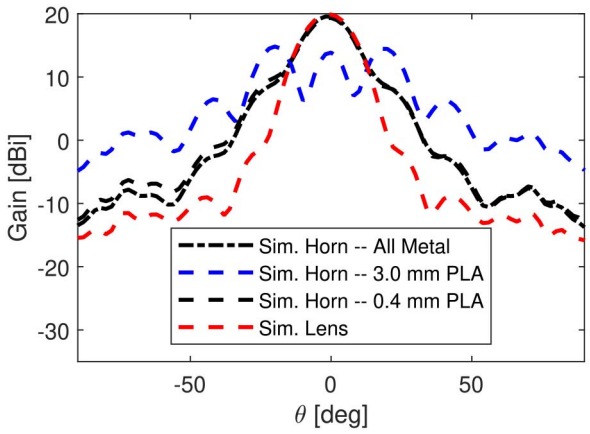

FIGURE 3. Simulated $\vec{E}$−Plane at 10 GHz.

To print the lens, the continuous function in Fig. 2 (b) was discretized into shells with a thickness of 3 mm to be electrically small, but large enough to easily FDM print each shell and the required cut-outs. Next, the permittivity gradient in Fig. 2 the density of the PLA was reduced with periodic cut-outs like in [7]. The cut outs in each shell of the lens are depicted in Fig. 5 and the relation between the cut size and relative permittivity is expressed in eqn. (13) where F is the volume ratio of air to PLA in each unit cell. Based on Fig. 2 a fill-volume-ratio F was found for

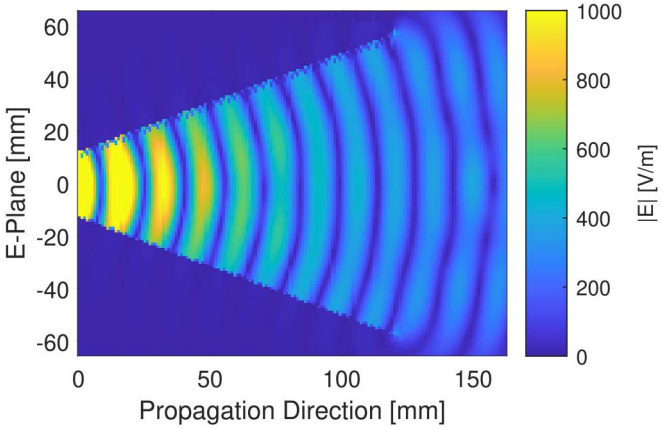

(a)

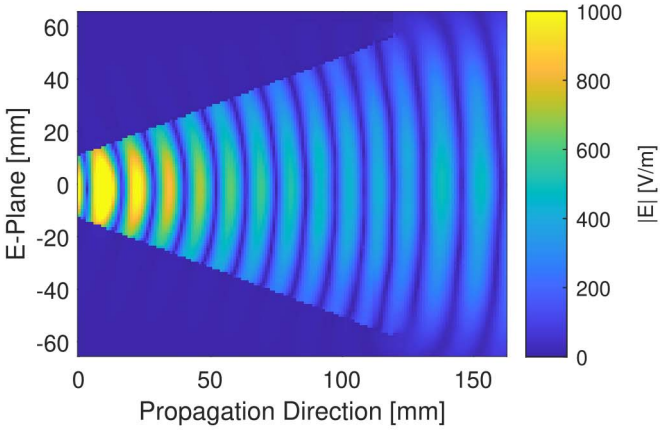

(b)

FIGURE 4. Field propagation through the (a) horn and the (b) lens at 10 GHz.

each shell and the cut outs were performed. These cut outs and shells were designed using a script-based CAD package called OpenSCad that allowed for repetitive parameterized cuts. The start position of each cut was varied on each shell so that the permittivity would be radially symmetric in all layers and would not align at a given point to produce a locally low or high region. After performing the desired cut outs on each shell, the shells were united to make the lens. To aid with printing, the lens was broken into the cone and dome sections, like was done when calculating the relative permittivity for each shell. This allowed the lens to be printed without support material as the cut plane could be used as the base of the print. Fig. 6 shows the cone and dome parts of the lens. After printing these two parts were centered using the hole through the center of the lens and were bonded at the edges using cyanoacrylate glue.

$$n_{cell} = \sqrt{\epsilon_{r_{PLA}}} F + n_0(1 - F) \tag{12}$$

$$\epsilon_r = (n_{cell})^2. \tag{13}$$

Horn Design – A circular conical horn was designed to be externally metalized. This was done so that the horn could

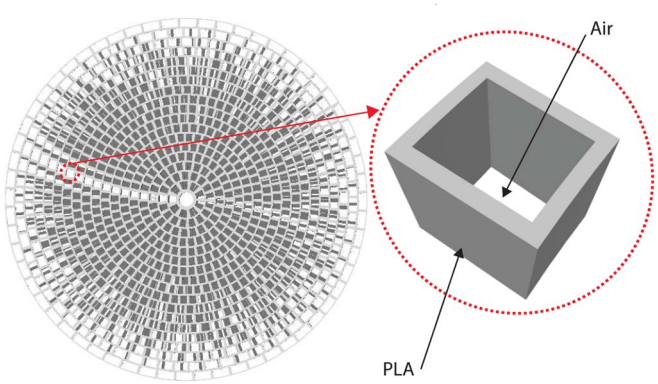

FIGURE 5. End view of the cone section of the lens highlighting a single unit cell to show how the permittivity is varied through the lens.

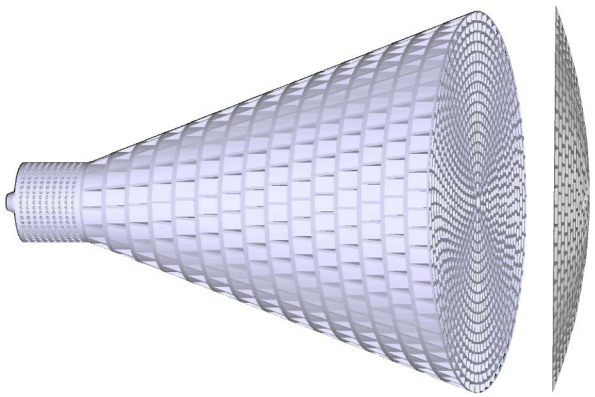

FIGURE 6. Printable model of the cone (left) and the dome (right) parts of the lens.

be printed in a single piece with foil applied on the outside to simplify the printing process and allow for the circular wave guide to be clamped into the transition without the need for an external flange. The final design is shown in Fig. 7. Normally, FDM prints must have a minimum wall thickness to be rigid and print successfully the minimum wall thickness is dependent on the printer and the structure. However, a non-electrically-small dielectric wall on the inside of the horn creates a lower impedance region near the metallization that can cause large side-lobes in the $\vec{E}$-plane. These side-lobes were seen in simulation comparison an externally metalized horn with 3 mm thick walls versus an all-metal horn as seen in Fig. 3. Through simulation it was determined that if the walls of the PLA on the inside of the metal were made thin enough, the effects of the PLA support would be minimal. Fig. 3 shows the simulated $\vec{E}$-plane radiation pattern at 10 GHz for the all-metal horn and a 0.4 mm thick PLA horn performing similarly to the all metal case.

The horn was designed to be printed with a thickness of 0.4 mm as shown in Fig. 7. To make this horn printable, it was printed in a continuous contour where the print-head gradually increases vertically while printing a single wall, commonly known as *vase mode*. This allowed for a thin wall without a rough seam or warped walls that was thinner than more expensive plastic printing options such as SLS of Nylon

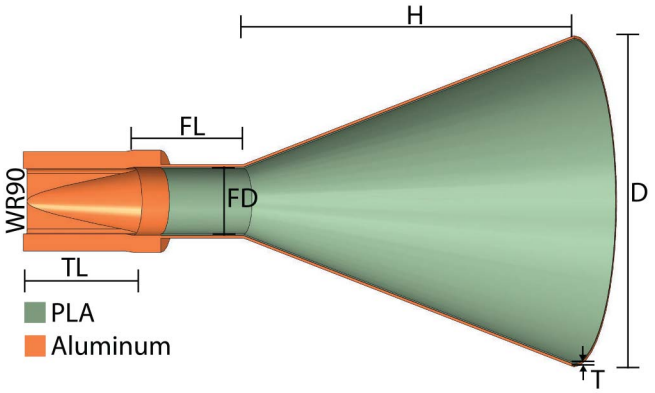

var.	TL	FL	FD	H	D	T
[mm]	40	25	23.83	120	114	0.4

FIGURE 7. Dimensioned model of the thin PLA horn.

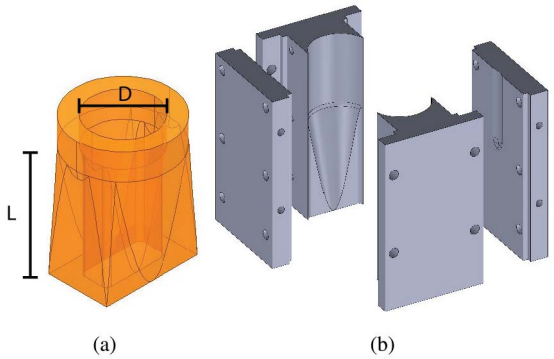

var.	L	D
[mm]	40	23.83

FIGURE 8. (a) Simulation model of the rectangular to circular waveguide transition, (b) Exploded view of the assembly of the printable transition model.

which was only able to produce a minimum wall thickness of 0.7 mm [5]. This works well for circular structures since the forces on the cooling print are evenly distributed so the print does not warp which allowed for a smooth and consistent print. The result is an extremely lightweight horn that is rigid enough to support itself and hold its shape.

Transition Design – A rectangular to circular transition needed to be designed to adapt WR90 rectangular waveguide to the circular feed of each antenna used in this work. This was done so that an off-the-shelf coaxial to rectangular waveguide launcher could be used as the feed. For this work a circular waveguide diameter of 23.83 mm was chosen as it has a has an operating bandwidth comparable to that of WR90. The transition was designed as a conical tapered transition between the rectangular and circular waveguide like the design in [23]. The launcher transmits a linearly polarized wave in the rectangular waveguide (TE_{10}) to the same polarization in the circular waveguide (TE_{11}). The transition can be visualized in Fig. 8. The gradual contour of the transition is easy to fabricate with 3D printing and allows for a better impedance match than step transitions like [24] that are easier to manufacture using traditional methods. Using a conical transition, the parameter that is tuned is the length of the transition which was chosen to give a good impedance match and minimize the total length.

The transition as designed in Fig. 8 (a) was printable, however, it would have been difficult to metalize the inside of the transition with foil while keeping the foil smooth. The transition was internally metalized to better match with the WR90 waveguide launcher and allow for thicker PLA walls needed for the structure of the transition. If this part were to be machined through traditional means, it would be broken down the broad wall and milled as two parts, however, to metalize a printed part, the foil would need to bend in multiple directions which would introduce wrinkles. To minimize the number of compound bends that were needed when applying the foil, the transition was broken into four parts at the corners of the rectangular waveguide as seen in Fig. 8 (b). To reassemble the transition after printing and metalizing, holes were included in the parts that could be thread-tapped for machine screws to secure the four parts together and to clamp onto the externally metalized circular waveguide to feed the horn and the lens.

III. MEASURED RESULTS

The transition, horn, and lens were all FDM printed using the method described. After printing each was metalized with aluminum foil tape with a thickness of 70 μm. To help smooth each print, all top surfaces were printed with *ironing*, a method where the hot end is moved over the part to smooth the top surface, this removed any need to sand to parts before metalizing. Fig. 9 (a) shows the metalized transition before assembly. The thin wall printed circular horn can be seen in Fig. 9 (b) showing the thin PLA wall with the external metallization. Fig. 9 (c) shows the fully assembled lens before taping and Fig. 9 (d) shows the metalized lens attached to the assembled waveguide transition. For the lens and the horn, the tape was applied in a spiral-like pattern around each cone to avoid wrinkles. Fig. 9 (d) shows the waffling pattern in the aluminum tape because of the gaps in the support of the lens. The mass of the fabricated: thin-walled horn is 23 g, lens is 287 g, and if the same horn were machined from copper with a wall thickness of 3 mm would have a mass of 785 g.

The measured and simulated input reflection results are compared in Fig. 10. An Anritsu MS4644B VNA was used with a WR90 calibration kit (A-INFO 90CLKA1) to set the reference plane after the WR90 launcher to match the simulation setup. The impedance bandwidth of both the conical GRIN lens and thin-wall horn antenna were better than -10 dB across the full rated bandwidth of WR90 (8.2 GHz to 12.4 GHz) and better than -15 dB above 8.8 GHz. There is reasonable agreement between the measured and simulated results. For each comparison, the measured thin-walled horn

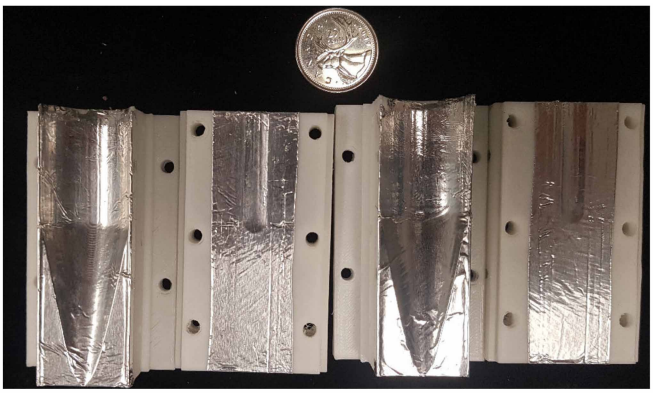

(a)

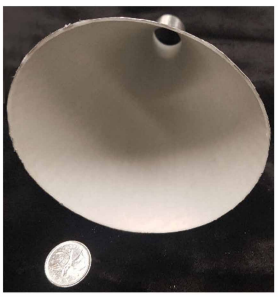

(b)

(c)

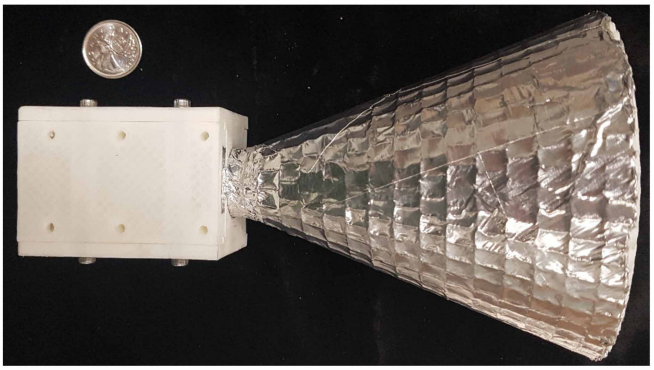

(d)

FIGURE 9. 3D printed and metalized horn and lens: (a) four sections of the rectangular to circular waveguide transition (b) 3D Printed horn showing thin PLA support structure (white) and aluminum tape metallization on the outside, (c) 3D printed lens before metallization with the dome attached to the cone, (d) assembled transition and metalized lens.

is compared to a simulation model that includes the thin PLA and one that is an ideal all metal horn to show the minimal impact of this thin PLA support and the thin PLA has much less of an effect in the measured results than it did in simulation.

Far-field measurements were performed in the anechoic chamber at Queen's University and realized gain was measured throughout and was calibrated using a TDK HRN-0118 reference horn antenna with ISO17025 calibration accreditation. The measured and simulated peak realized gain are shown in Fig. 11 showing good agreement between measurement and simulation with both the

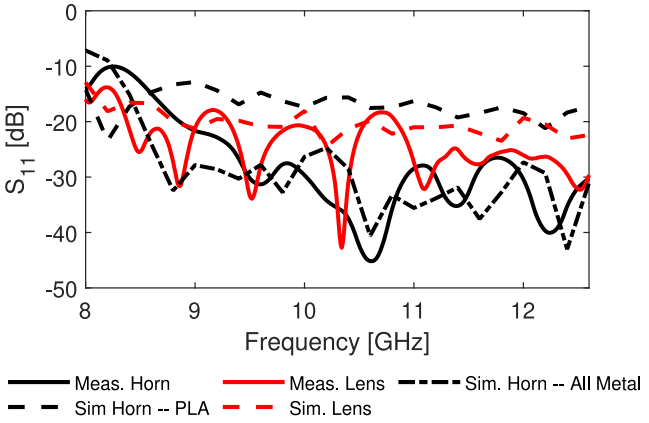

FIGURE 10. Measured and simulated input reflection, both using a reference plane as the start of the 3D printed rectangular waveguide, showing an input reflection better than −10 dB across the full WR-90 operating band.

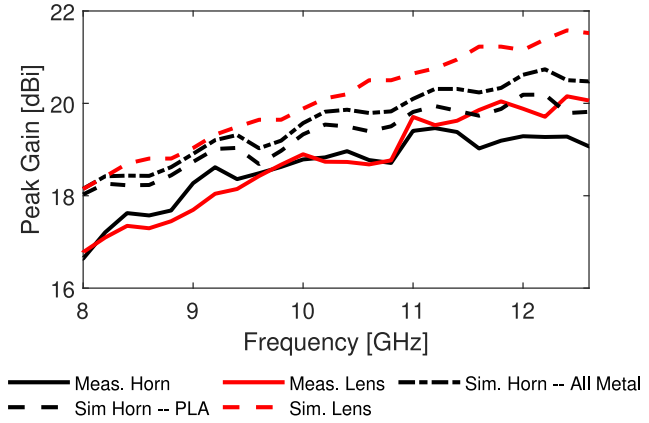

FIGURE 11. Measured and simulated peak realized gain. Gain linearly increases across the band with a total variation of less than 1.5 dB.

lens and the horn showing 18.7 dBi of peak gain at mid-band. The slight difference in peak-gain between measurement and simulation can be attributed to un-modeled loses in the PLA, and the losses through the WR90 to coaxial launchers.

Normalized radiation patterns for the two-principal cuts in the $\vec{E}$ and $\vec{H}$ planes across the band are shown in Fig. 12. The radiation patterns here are normalized to show the SLL reduction in the $\vec{E}$ provided by the lens. In the $\vec{H}$-plane the lens performs very similarly to the horn or manages to slightly improve the SLL. Additionally, there is good agreements between the measured and simulated beam-shape in all setups including for the horn between the simulation model with and without the PLA support, confirming that if the support can be printed thin enough, it will have minimal impact on the performance of the horn.

The full SLL improvement of the lens over the horn is shown in Fig. 13. The lens improves the $\vec{E}$-plane SLL by a minimum of 10 dB across the band and by 15 dB at mid-band. This is the best-case SLL improvement seen

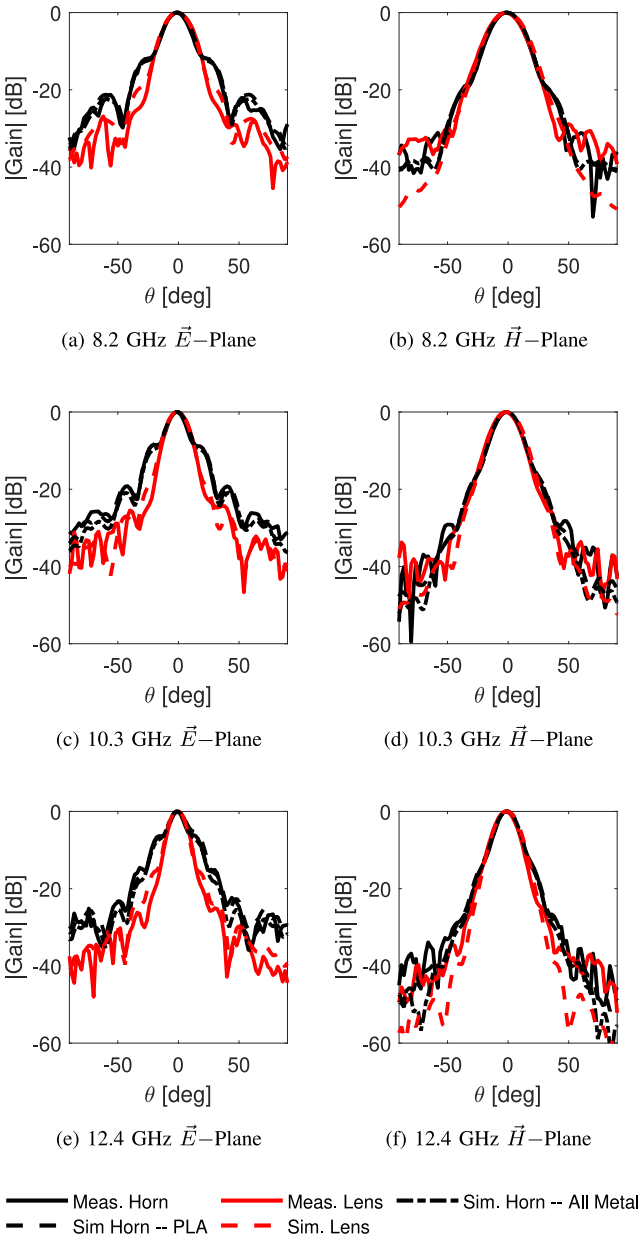

FIGURE 12. Normalized gain patterns across the operating band of the horn and lens antennas. Measured and simulated results are presented, refer to Fig. 11 for realized gain at boresight.

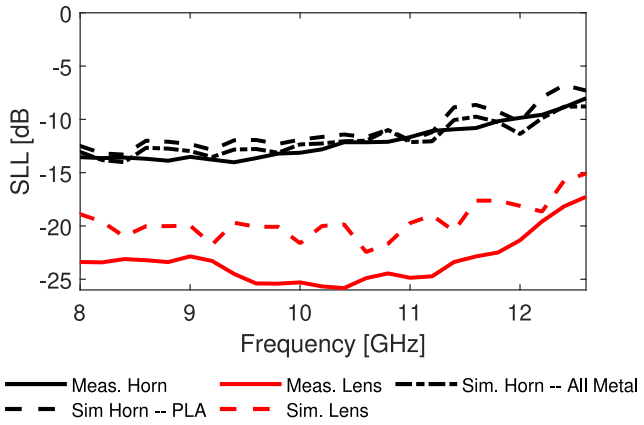

FIGURE 13. Measured and simulated side lobes in the $\vec{E}$-Plane across the band. At mid-band, the lens provides over a 10 dB reduction in SLL.

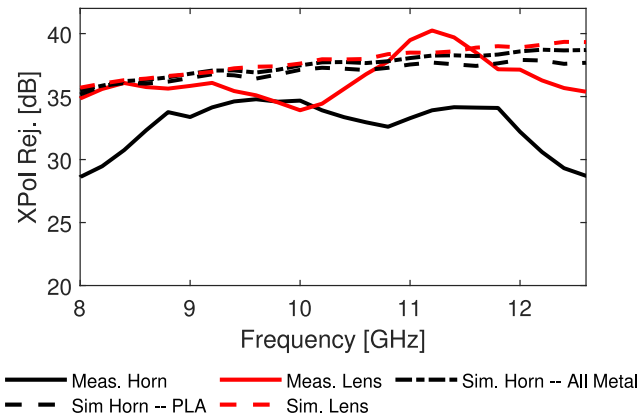

FIGURE 14. Measured and simulated cross polarization rejection at boresight for both the horn and the lens.

TABLE 1. Comparison table between this work and other 3D printed lensed antennas.

Ref.	Antenna Topology	Gain (dBi)	$\vec{E}$-SLL (dB)	BW (GHz)	App. Eff. (%)
This Lens	3D Printed Lens	18.7	25	8.2–12.4	49
This Thin PLA	3D Printed Horn	18.7	10	8.2–12.4	49
[5]	GRIN lens in horn	16	25	7.5–18	63*
[10]	GRIN lens fed patch antenna	17.7	-	10–12.4	36
[13]	WG fed Mikaelian Lens	18.9	15	8.5–12	-

* Compared to standard gain horn

with other lenses integrated into horns [5]; however, this lens is easier to construct as the lens also acts as the support for the external metallization and no other structure is needed.

The measured and simulated cross-polarization rejection at boresight are shown in Fig. 14. For each antenna the measured and simulated cross-polarization rejection is above 27 dB across the band.

A comparison table is shown in Table 1 that compares the lens and horn from this work to other similar works in terms of peak gain, SLL, bandwidth, and aperture efficiency.

IV. CONCLUSION

In this work a 3D printed conical GRIN lens was presented that functioned as the support for external metallization and improved the SLL in the $\vec{E}$-plane that is a common issue with all linearly polarized aperture antennas. Further

validation was given to the method of FDM 3D printing waveguide components from plastic and metalizing the parts with aluminum tape. This method of production provides both light-weight and inexpensive to prototype waveguide components and considered ease of metallization with foil tape throughout the design. A rectangular to circular waveguide transition, a thin walled externally metalized circular horn antenna, and a conical GRIN lens that also functioned as the support for the lens all showed measured performance that agreed with simulation.

ACKNOWLEDGMENT

I. Goode is a recipient of the Ontario Graduate Scholarship from the Province of Ontario, Canada, the Ian M. Drum Scholarship at Queen's University, and NSERC PGS-D from the Government of Canada.

REFERENCES

[1] G.-L. Huang, S.-G. Zhou, C.-Y.-D. Sim, T.-H. Chio, and T. Yuan, "Lightweight perforated waveguide structure realized by 3-D printing for RF applications," *IEEE Trans. Antennas Propag.*, vol. 65, no. 8, pp. 3897–3904, Aug. 2017.

[2] A. H. Wahyudi, J. T. S. Sumantyo, S. Wijaya, and A. Munir, "PLA-based 3D printed circularly polarized X-band horn array antenna for CP-SAR sensor," in *Proc. Int. Workshop Antenna Technol.*, 2018, pp. 1–4.

[3] K. V. Hoel, S. Kristoffersen, J. Moen, G. Holm, and T. S. Lande, "Characterization of a 3D printed wideband waveguide and horn antenna structure embedded in a UAV wing," in *Proc. IEEE 10th Eur. Conf. Antennas Propag.*, 2016, pp. 1–4.

[4] M. Dionigi, C. Tomassoni, G. Venanzoni, and R. Sorrentino, "Simple high-performance metal-plating procedure for stereolithographically 3-D-printed waveguide components," *IEEE Microw. Wireless Compon. Lett.*, vol. 27, no. 11, pp. 953–955, Nov. 2017.

[5] K. V. Hoel, M. Ignatenko, S. Kristoffersen, E. Lier, and D. S. Filipovic, "3-D printed monolithic GRIN dielectric-loaded double-ridged horn antennas," *IEEE Trans. Antennas Propag.*, vol. 68, no. 1, pp. 533–539, Jan. 2020.

[6] F. Pizarro, R. Salazar, E. Rajo-Iglesias, M. Rodriguez, S. Fingerhuth, and G. Hermosilla, "Parametric study of 3D additive printing parameters using conductive filaments on microwave topologies," *IEEE Access*, vol. 7, pp. 106814–106823, 2019.

[7] I. Goode and C. E. Saavedra, "3D printed 18 GHz to 28 GHz horn antenna and gradient index of refraction lens," in *Proc. Gen. Assem. Sci. Symp. Int. Union Radio Sci.*, 2021, pp. 1–4.

[8] D. Helena, A. Ramos, T. Varum, and J. N. Matos, "Inexpensive 3d-printed radiating horns for customary things in IoT scenarios," in *Proc. 14th Eur. Conf. Antennas Propag.*, 2020, pp. 1–4.

[9] H. Yao, S. Sharma, R. Henderson, S. Ashrafi, and D. MacFarlane, "Ka band 3D printed horn antennas," in *Proc. Texas Symp. Wireless Microw. Circuits Syst.*, 2017, pp. 1–4.

[10] T. Hayat, M. U. Afzal, F. Ahmed, S. Zhang, K. P. Esselle, and J. Vardaxoglou, "The use of a pair of 3D-printed near field superstructures to steer an antenna beam in elevation and azimuth," *IEEE Access*, vol. 9, pp. 153995–154010, 2021.

[11] C. Turkmen and M. Secmen, "Dual-band omnidirectional and circularly polarized slotted waveguide array antenna for satellite telemetry and telecommand," *IEEE Antennas Wireless Propag. Lett.*, vol. 20, pp. 2100–2104, 2021.

[12] Y. Li, L. Ge, M. Chen, Z. Zhang, Z. Li, and J. Wang, "Multibeam 3-D-printed Luneburg lens fed by magnetoelectric dipole antennas for millimeter-wave MIMO applications," *IEEE Trans. Antennas Propag.*, vol. 67, no. 5, pp. 2923–2933, May 2019.

[13] W. Shao and Q. Chen, "2-D beam-steerable generalized Mikaelian lens with unique flat-shape characteristic," *IEEE Antennas Wireless Propag. Lett.*, vol. 20, pp. 2033–2037, 2021.

[14] X. Wang, Y. Cheng, and Y. Dong, "A wideband PCB-stacked air-filled Luneburg lens antenna for 5G millimeter-wave applications," *IEEE Antennas Wireless Propag. Lett.*, vol. 20, pp. 327–331, 2021.

[15] R. Cicchetti, V. Cicchetti, A. Faraone, and O. Testa, "A class of lightweight spherical-axicon dielectric lenses for high gain wideband antennas," *IEEE Access*, vol. 9, pp. 151873–151887, 2021.

[16] G. H. Lee, S. Kumar, H. C. Choi, and K. W. Kim, "Wideband high-gain double-sided dielectric lens integrated with a dual-bowtie antenna," *IEEE Antennas Wireless Propag. Lett.*, vol. 20, pp. 293–297, 2021.

[17] M. F. Farooqui and A. Shamim, "3-D inkjet-printed helical antenna with integrated lens," *IEEE Antennas Wireless Propag. Lett.*, vol. 16, pp. 800–803, 2016.

[18] M. Amiri, F. Tofigh, A. Ghafoorzadeh-Yazdi, and M. Abolhasan, "Exponential antipodal Vivaldi antenna with exponential dielectric lens," *IEEE Antennas Wireless Propag. Lett.*, vol. 16, pp. 1792–1795, 2017.

[19] K. Liu, C. Zhao, S.-W. Qu, Y. Chen, J. Hu, and S. Yang, "A 3-D-printed multibeam spherical lens antenna with ultrawide-angle coverage," *IEEE Antennas Wireless Propag. Lett.*, vol. 20, pp. 411–415, 2021.

[20] Y.-X. Zhang, Y.-C. Jiao, and S.-B. Liu, "3-D-printed comb mushroom-like dielectric lens for stable gain enhancement of printed log-periodic dipole array," *IEEE Antennas Wireless Propag. Lett.*, vol. 17, pp. 2099–2103, 2018.

[21] I. Goode and C. E. Saavedra, "Millimeter-wave beam-steering antenna using a fluidically reconfigurable lens," *IEEE Trans. Antennas Propag.*, vol. 69, no. 2, pp. 683–688, Feb. 2021.

[22] H. Banting and C. E. Saavedra, "Dielectric spectroscopy of fluids and polymers for microwave microfluidic circuits and antennas," *IEEE Trans. Microw. Theory Techn.*, vol. 69, no. 1, pp. 337–343, Jan. 2021.

[23] J. Strycharz and P. Piasecki, "3D printed circular and rectangular waveguide mode converters," in *Proc. 22nd Int. Microw. Radar Conf.*, 2018, pp. 24–28.

[24] E. L. Holzman, "A simple circular-to-rectangular waveguide transition," *IEEE Microw. Wireless Compon. Lett.*, vol. 15, no. 1, pp. 25–26, Jan. 2005.

IAN GOODE received the B.A.Sc. degree in engineering physics with an Electrical Engineering sub-option from Queen's University in 2017, where he is currently pursuing the Ph.D. degree with the Department of Electrical Engineering. He was the Chief Technical Officer of Rover Design for the Queen's Space Engineering Team (QSET) from 2016 to 2018, where he oversaw the full redevelopment of QSET's Mars Rover prototype that competed with the University Rover Challenge. His current research interests include lensed antennas, low-cost additive manufacturing and metallization methods for RF and microwave systems, and antenna measurement systems. He has received multiple scholarships to support his graduate work, including the Ian M. Drum Scholarship, the Ontario Graduate Scholarship, and NSERC PGS-D. He was a recipient of the 2019 IEEE Kingston Section M.A.Sc Research Excellence Award and the 2021 URSI Young Scientist Award.

CARLOS E. SAAVEDRA received the B.Sc. degree in electrical engineering from the University of Virginia and the M.Sc. and Ph.D. degrees in electrical engineering from Cornell University, Ithaca, NY, USA. He is a Registered Professional Engineer (P.Eng.) in the province of Ontario, Canada. He is currently a Full Professor and the Head of the Department of Electrical and Computer Engineering, Queen's University, Kingston. On Sabbatical leaves he has held visiting appointments with the University of Navarra (Tecnun), San Sebastian, Spain; the Universidade Federal of Rio Grande do Sul, Brazil; and the University of Twente, Holland. He has served as the Co-Chair for the Natural Sciences and Engineering Research Council of Canada Discovery Grant Evaluation Group 1510 and has also served on grant review panels at the U.S. National Science Foundation. He is a Former Associate Editor of the IEEE TRANSACTIONS ON MICROWAVE THEORY AND TECHNIQUES and a Guest Editor of the IEEE OPEN JOURNAL OF ANTENNAS AND PROPAGATION and the *IEEE Microwave Magazine*.